In-Situ Observations of Oxidation and Phase Stability in Cast Nickel-Based Intermetallic Alloys

S.S. BABU, E.D. SPECHT, M.L. SANTELLA, G.E. ICE, and S.A. DAVID

The effects of the as-cast microstructure on the oxidation characteristics of two Ni-Al-Cr alloys with either γ or γ' primary solidification were investigated with an *in-situ*, time-resolved X-ray diffraction (TRXRD) technique using synchrotron radiation. The measurements, carried out during rapid heating and cooling, showed that a segregated microstructure in these cast alloys leads to the preferential formation of zirconium oxide before the formation of aluminum oxides is detected. The oxidation leads to a change in the phase stability and to the modification of surface microstructures. Computational thermodynamic models were used to explain the preferential formation of oxides in the as-cast microstructure.

I. INTRODUCTION

IN the last two decades, extensive research has been performed to develop nickel-based intermetallic alloys with high volume fractions of $L1_2$ ordered γ' phase, which are referred as Ni_3Al alloys.[1] The applications for which these alloys have been evaluated include transfer rolls, heat-treating trays, rails for walking beam furnaces, radiant burner applications, grate bars in calcination furnaces, and forging of die-blocks. Most of these applications require good strength properties in the range of 700 °C to 1200 °C and resistance to thermal cycling, as well as resistance to either severely oxidizing or carburizing atmospheres. There has been extensive applied research to describe the performance of Ni_3Al alloys for these conditions.

Research on the oxidation of nickel-based superalloys has been done with reference to gas turbine applications.[2] The present work is part of the ongoing efforts to extend this knowledge to high-volume-fraction γ' alloys close to the Ni_3Al composition. Previous work on Ni_3Al alloys has indicated that the oxidation resistance of these alloys is generally good compared to other nickel-based alloys.[3,4] However, the effects of processing, oxidation environment, and thermal cycling are yet to be quantified completely. Recent research has focused on the high-temperature corrosion behavior of these alloys under static and cyclic conditions in different atmospheres.[5] Klower *et al.* studied the stability of these alloys in carburizing, chlorinating, and sulfidizing environments. Their work showed that the Zr-containing alloys oxidized heavily through internal oxidation of Zr-rich regions. Lee *et al.* studied interactions between phase stability and the types of oxides that form in the oxidizing conditions at temperatures of 900 °C to 1100 °C.[6,7] Their results were in agreement with those of Klower.[6] In addition, Lee *et al.*[7] related the preferential formation of oxides to the solidification segregation. It is important to note that there exists a good knowledge base on the oxidation characteristics of intermetallic alloys.[8,9,10] The main interest in the present article is to evaluate the interaction between phase stability and the early stages of oxidation during rapid heating and cooling.

Based on these previous studies, it was speculated that the early stages of oxidation under rapid thermal cycling might be influenced both by the primary mode of solidification and by the relative stability of various phases that form during solidification. For example, in alloys containing aluminum concentrations close to 20 at. pct, the primary solidification will occur by the formation of γ' phase, and the γ phase will form at the interdendritic regions. In contrast, in alloys containing less aluminum, the primary solidification will occur by γ phase, and a eutectic mixture containing coarse γ' will form in the interdendritic regions. It is important to note that the associated segregation and phase balance may affect the early stages of oxidation. Traditional high-temperature X-ray diffraction (XRD) methods have been used before to study the oxidation kinetics.[11] To allow for good time resolution, synchrotron radiation has been used to measure the growth stresses in the oxide layers.[12,13] In the work presented here, we used synchrotron radiation to obtain diffraction data at 2-second intervals for rapid measurement of phase stability and oxide formation during rapid thermal cycling. The results emphasize *in-situ* determination of the sequences of oxide formation during heating and cooling. The goal of these characterizations is to understand the effect of solidification mode as well as the change in composition of the alloy on the early stages of oxidation characteristics.

II. EXPERIMENTAL TECHNIQUES

Two Ni-Cr-Al ingots were prepared from pure charge materials by vacuum arc melting and casting into 70-mm-diameter × 150-mm-long copper molds. The alloy with the higher aluminum concentration will be referred as the Ni_3Al alloy, and the alloy with the lower aluminum concentration will be referred as the IC221M alloy. The nominal compositions of the two alloys are given Table I. For *in-situ* XRD investigations, the samples were cut from these ingots using the electrical discharge machining method. The samples were ground with fine mechanical polishing to a surface finish of 1 μm. No other special surface preparation such as chemical

S.S. BABU, formerly with the Metals and Ceramics Division, Oak Ridge National Laboratory, is with the Edison Welding Institute, Columbus, OH 43221. Contact e-mail: suresh_babu@ewi.org E.D. SPECHT, M.L. SANTELLA, G.E. ICE, and S.A. DAVID are with the Metals and Ceramics Division, Oak Ridge National Laboratory, Oak Ridge, TN 37831-6096.

Manuscript submitted April 15, 2005.

U.S. GOVERNMENT WORK
NOT PROTECTED BY U.S. COPYRIGHT

or electrolytic etching was done to these alloys before the investigation, to avoid any preferential etching of the surface. The test samples were in the form of bars 100-mm long, 4.5-mm wide, and 2-mm thick.

The samples were subjected to rapid heating and cooling heat treatments in air while *in-situ* time-resolved X-ray diffraction (TRXRD) was being performed in the synchrotron beam line. A resistive heating method was used to heat the samples in a preprogrammed cycle. All the samples were heated to 1250 °C at rates of 0.5 °C/s, 1 °C/s, 10 °C/s, and 50 °C/s using programmable control. These conditions will be referred as R0.5, R1, R10, and R50 throughout this article. The extreme conditions R0.5 and R50 will be discussed in detail. In the case of slow heating and cooling at 0.5 °C/s, the samples were isothermally held at 1250 °C for 10 minutes before the cooling cycle. The cooling rates for all samples were also programmed at the same level as heating rates. To avoid the spallation of surface oxides, only natural air cooling was used. As a consequence, the cooling rate of 50 °C could not be fully realized.

The X-rays, with wavelength of $\lambda = 0.041328$ nm, were provided by the UNICAT X-33 undulator beam line at the Advanced Photon Source (Argonne National Laboratory, Argonne, IL, USA). The X-rays were incident at a 6-deg glancing angle. The effective penetration depth is 8.2 μm, so the measurements are sensitive to surface oxidation kinetics during heating and cooling. A two-dimensional (2-D) image of the diffracted X-rays was recorded approximately every 2 seconds. Diffracted X-rays were recorded by a Princeton Instruments model SCX-1242E close-coupled device camera with 1024 × 1024 pixels, a 0.060 × 0.060 mm pixel size, and 16-bit resolution. The detector was placed 235 mm from the sample. The 2-D diffraction rings were summed to obtain intensity *vs* 2θ intensity plots. A schematic illustration of the experimental setup is shown in Figure 1. Details of the same technique for other alloy systems are published elsewhere.[14] The data were analyzed with user-written computer programs and peak-analysis modules in a commercial plotting package. The TRXRD data were obtained during the R0.5 and R50 experiments from both the IC221M and Ni_3Al alloys. The surfaces of the samples were examined before and after TRXRD experiments, using the conventional XRD technique with Cu K_α radiation to verify the presence of different phases and oxides.

Specimens in the as-received and heat-treated conditions were also examined metallographically using Aquaregia solution to delineate the microstructure.

Table I. Nominal Alloy Compositions in Wt Pct

Alloy		Al	Cr	Mo	Zr	B	Balance
IC221M	Wt Pct	8.0	7.7	1.5	1.7	0.008	Nickel
	At. Pct	15.9	7.95	0.84	1.0	0.004	
Ni_3Al	Wt Pct	12.0	4.0	1.5	0.8	0.008	Nickel
	At. Pct	22.94	3.97	0.80	0.45	0.004	

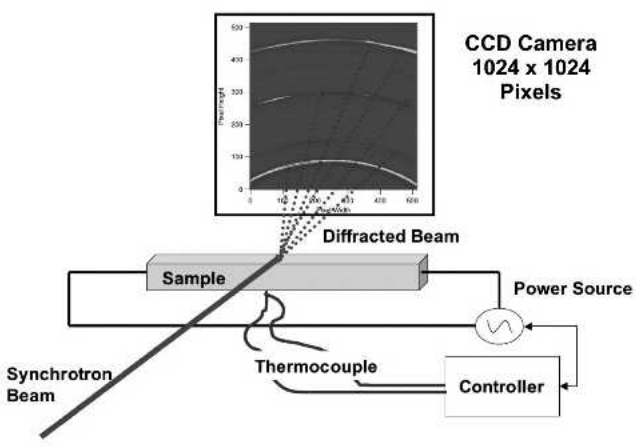

Fig. 1—Schematic illustration of the TRXRD experimental setup used in the current work.

III. RESULTS

A. *As-Cast Microstructure*

Initial observations of the IC221M and Ni_3Al samples before the *in-situ* oxidation are shown in Figures 2 and 3. The macrophotographs show as-cast structures containing primary dendrites and darkly etching interdendritic regions in both the samples. Figure 2(b) indicates that the microstructure of the IC221M alloy consisted of a very fine distribution of γ' precipitates within the γ dendritic cores and coarse γ' phase near the eutectic regions. The XRD results showed the presence of both an fcc and $L1_2$ ordered structure, confirming that both the γ and γ' phases were present. A darkly etching phase, presumed to be Ni_5Zr phase, was also observed in the IC221M microstructure. However, the XRD did not show any peaks from this phase, possibly due to its small volume fraction.

High-magnification examination revealed that the microstructure of the Ni_3Al alloy was indeed different from that of IC221M alloy. The optical metallography showed the presence of brightly imaging γ' dendritic grains and the presence of darkly etching γ phase in between the den-

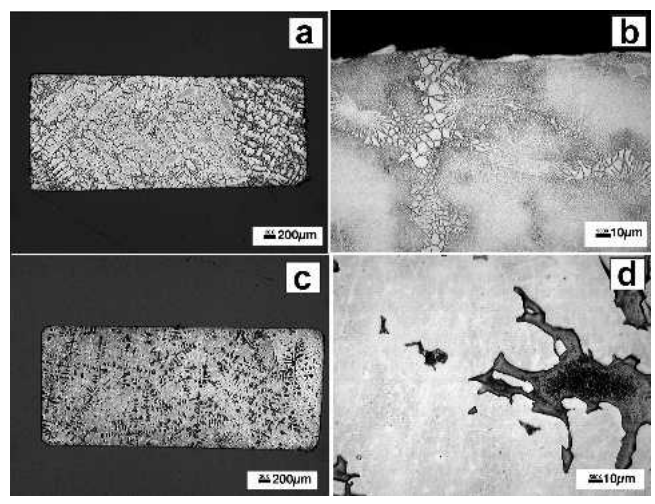

Fig. 2—Overview of the as-cast microstructure after etching with aquaregia solution: (*a*) low-magnification cross-sectional micrograph of the sample from IC221M, (*b*) high-magnification micrograph of the IC221M sample near the surface, showing the presence of an interdendritic microstrutcure, (*c*) low-magnification cross-sectional micrograph of the sample from the Ni_3Al alloy, and (*d*) microstructure near the surface of the Ni_3Al sample, showing the presence of darkly etching γ regions with fine features in the middle.

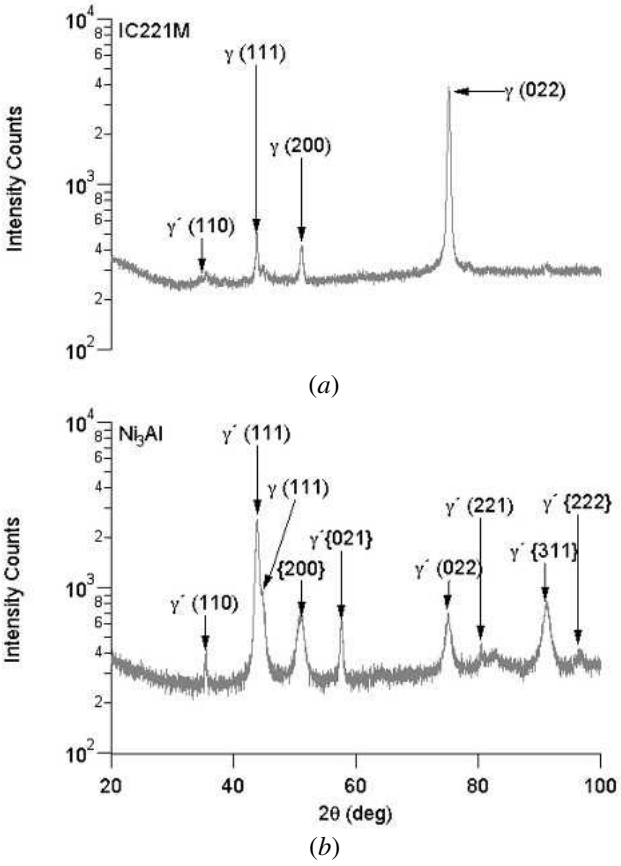

Fig. 3—XRD measurements using Cu K_α radiation from (*a*) the IC221M alloy and (*b*) the Ni_3Al alloy.

dritic grains (Figures 2(c) and (d)). The XRD results show that the predominant phase in the Ni_3Al alloys is $L1_2$ ordered γ' phase (Figure 3(b)). The splitting of the {111} reflection confirmed that the fcc γ phase was also present. It is important to note that Klower[6] found very fine disordered γ phase within the γ' phase. However, our XRD results cannot distinguish these two forms of γ phase. These results showed that with these alloys, two different initial microstructures have been attained through casting processes and by changing the compositions.

B. *Time-Resolved XRD Results*

The *in-situ* TRXRD results from the surfaces of both the Ni_3Al and IC221M during the R0.5 and R50 experiements are presented in Figure 4. The plots show the diffracted intensity in terms of color gradients as a function of 2θ diffraction angle and time. The plots also show the corresponding temperature changes. The diffraction peaks were identified by comparing the measured peaks at room temperature to standard published diffraction spectra. Most of the peaks were identified using numerical techniques from the data presented in Figure 4. In certain cases, the peaks are not identified uniquely in the 2θ range from 14 to 18, due to overlap of diffraction peaks from different oxides. Due to the overlap of the diffraction peaks, only qualitative analysis is possible, and relative fractions of different oxides cannot be deduced.

The plots show gradual shifts of all diffraction peaks to lower 2θ values with an increase in temperature to peak temperature and a gradual decreased shift to higher 2θ values with a decrease in temperature. This is a typical behavior due, respectively, to thermal expansion and contraction of the lattice. The diffraction data show that both γ and γ' are present in both alloys, similar to the room-temperature measurements shown in Figure 3. Splitting of the {111} peaks was observed in all the cases, indicating the overlap of the diffraction peaks from the γ and γ' phases. However, due to the variation of the lattice parameter with temperature and possible diffusion of elements between these phases, the volume fractions of γ and γ' could not be deconvoluted using these {111} reflections. Therefore, the (211) superlattice reflection was used to monitor the changes in the γ' fraction during heating and cooling. In the case of the IC221M alloys, during heating, a transition from a primary γ' phase with a small lattice parameter to that with a large lattice parameter was observed. The details of the analysis will be presented later. The data also revealed the presence of two types of zirconium oxides, *i.e.*, a low-temperature monoclinic form[15] and a high-temperature tetragonal form.[16] The low-temperature form is referred to as ZrO_2(LT), and the high-temperature form is referred to as ZrO_2(HT) throughout this article. In addition, the presence of corundum (Al_2O_3) was also detected in all cases except for the R50 experiment with the Ni_3Al alloy.

At rapid heating and cooling conditions, the extent of oxide formation in the Ni_3Al alloy was minimal. Interestingly, the diffraction data from the Ni_3Al alloys showed anomalous peaks close to primary γ' (211), which appear and disappear during heating (Figures 5(a) and (b)) in the temperature range of 800 °C to 1200 °C. This metastable γ' diffraction always appeared with a smaller lattice parameter than that of the primary γ' phase for both slow and rapid heating rates. The origin of this diffraction could be due to metastable γ' within the γ phase in the interdendritic regions,[6] which eventually dissolves at higher temperatures. Further work is necessary to understand this metastable γ' phase.

In the next step, the interaction of oxide formation and phase stability for both alloys subjected to the R0.5 and R50 heat treatments were evaluated. The areas under different diffraction peaks were calculated using numerical methods.[14] To allow for analyses without overlap from different peaks, the analyses were limited to the (101) peak of the high-temperature tetragonal ZrO_2 phase, the $(\bar{1}11)$ peak of the low-temperature monoclinic ZrO_2 phase, the (214) peak of corundum, the (111) peak representing both γ and γ' phase, and the (211) peak of the γ' phase (Figures 6(a) through (d)).

In the case of the R0.5 experiment on the IC221M alloy (Figure 6(a)), while heating above 750 °C, the area fraction of ZrO_2(HT) increased. With continued heating above 830 °C, the transition from a predominant primary γ'-phase (211) diffraction peak to a predominant secondary γ'-phase (211) diffraction peak with a larger lattice parameter was observed. This also coincides with the rapid increase in the formation of ZrO_2(HT). Heating above 1130 °C leads to the disappearance of the primary γ' phase. At and above 930 °C, the diffraction peaks from the ZrO_2(LT) appeared and increased slightly. However, on heating above 1160 °C, the diffraction peaks from ZrO_2(LT) disappeared. At 1200 °C, the formation of corundum (Al_2O_3) was observed. With continued

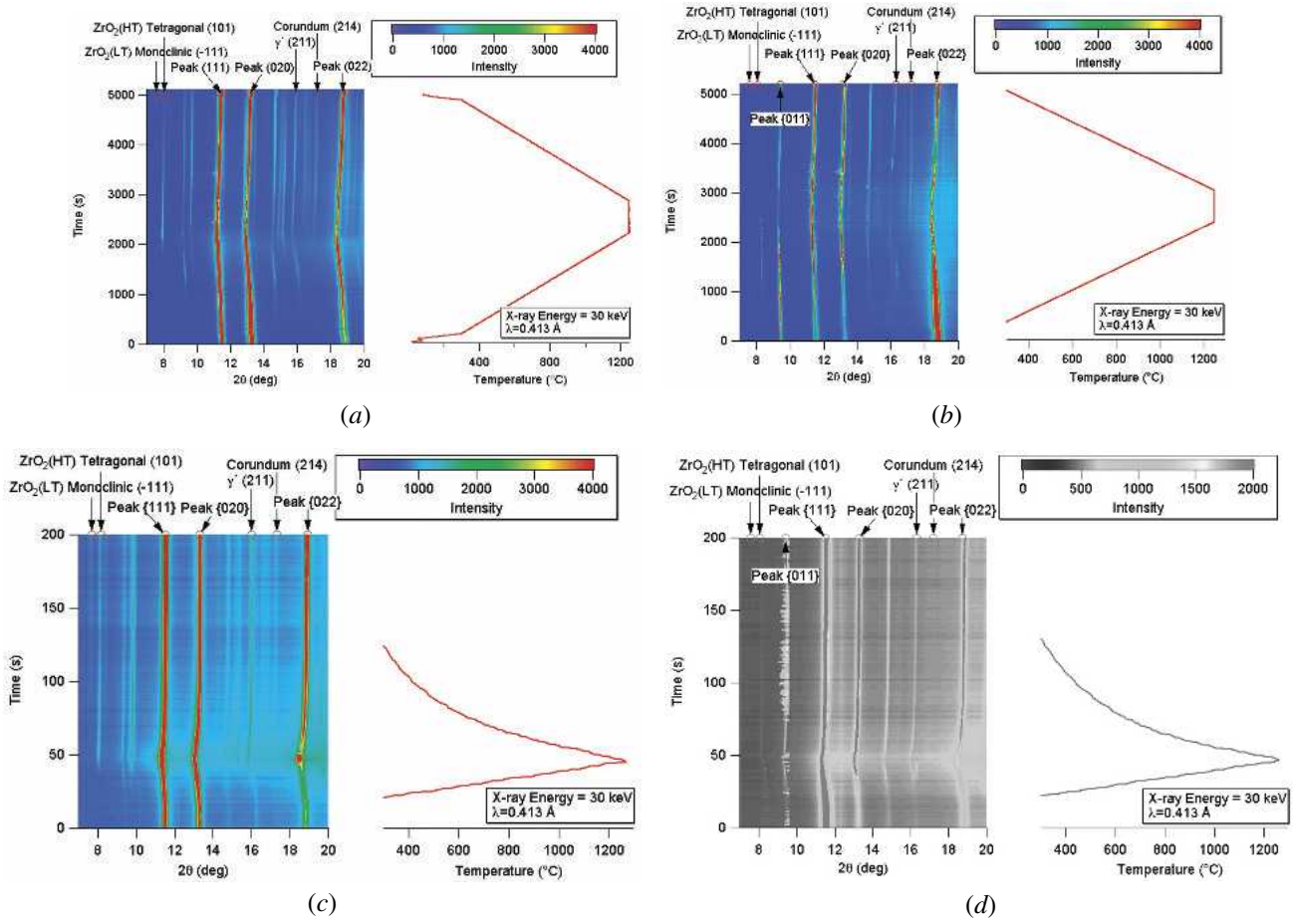

Fig. 4—Overview of the TRXRD results: (*a*) and (*b*) the IC221M and Ni_3Al alloys, respectively, subjected to heating and cooling at a rate of 0.5 Ks^{-1}, and (*c*) and (*d*) the IC221M and Ni_3Al alloys, respectively, subjected to heating and cooling at a rate of 50 Ks^{-1}. In the images, the background intensity is given by the blue color and the peak intensity is given by the red color.

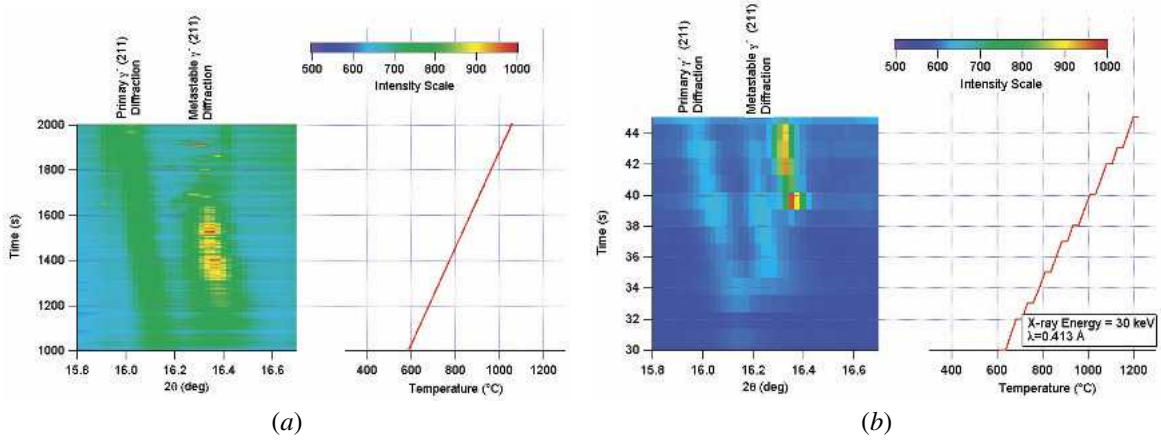

Fig. 5—Magnified section of the TRXRD data from Ni_3Al alloys subjected to (*a*) the R0.5 experiment and (*b*) the R50 experiment, showing the formation and disappearance of metastable γ' phase.

heating and holding at 1250 °C, the peak area of corundum increased, indicating growth of an external Al_2O_3 scale. This increase in Al_2O_3 peak area coincided with the decrease in volume fraction of ZrO_2(HT). The peak area fraction of the secondary γ' phase did not change during holding or even during cooling. The area of the Al_2O_3 peak area continued to increase even during cooling and reached a plateau at around 800 °C. On cooling below 830 °C, the diffraction peak from ZrO_2(LT) reappeared and continued to grow at the expense of the ZrO_2(HT) diffraction peak.

At 1200 °C and above, the fcc diffraction rapidly changes from rings of diffraction to a few very intense spots, corresponding to grain growth and increased crystalline perfection. As a result, the diffracted area under the fcc (111) peaks

is no longer statistically significant. This appears not to affect the $L1_2$ phases, which retain a small grain size. The aforementioned data indicated that there exists a strong interaction between phase stability and the early stages of oxidation. It is of interest to compare these measurements with those measured from the Ni_3Al alloys.

The data from the Ni_3Al alloys during the R0.5 experiment (Figure 6(b)) showed a faint presence of ZrO_2(HT) even at the initial stages. This is attributed to the formation of a thin ZrO_2 surface-oxide layer during sample preparation. An overview of the data from the Ni_3Al alloys showed that the diffraction-peak intensities from oxides were slightly lower than those of the IC221M alloy. With the start of the heating cycle, the area under the ZrO_2(HT) diffraction peak increased and reached a peak value at approximately 850 °C. With continued heating, the peak area reduced, with a large scatter in the data. The diffraction peaks from the ZrO_2(LT) were observed for the first time on heating above 1024 °C. Interestingly, continued heating above this temperature to 1250 °C did not lead to the disappearance of this phase. At and above 1180 °C, the formation of Al_2O_3 was observed. Similar to the IC221M alloy, the formation of Al_2O_3 continued even during isothermal holding at 1250 °C and cooling. In contrast to the IC221M alloy, the diffraction peaks from ZrO_2(HT) completely disappeared in the Ni_3Al alloys on holding at 1250 °C. In this alloy, the transition from a primary γ' to secondary γ' phase was not observed. The peak area under the (211) γ' diffraction peak remained constant for most of the heating part of the experiment and slightly increased during cooling. In the analysis of the data, the anomalous (211) diffraction peak was not considered due to the difficulties in fitting the peak shapes during analysis. The presence of a (111) diffraction split was observed at the early stages of heating, possibly due to the presence of the disordered γ phase; the quantification of the same was not done due to overlapping diffraction peaks. Nevertheless, the split disappeared on heating the sample above 1150 °C. In general, the oxidation characteristics of the Ni_3Al alloys appear to be similar to those of the IC221M alloy, except for the temperatures of the formation. It is of interest to compare these results with the rapid heating and cooling conditions.

In case of the R50 experiment on the IC221M alloy (Figure 6(c)), the splitting of the (211) peak was observed earlier on, from 500 °C. However, the extent of the split was not as pronounced as that of the results from the R0.5 experiment. On heating above 1100 °C, the separation between these peaks vanished and a single peak appeared. However,

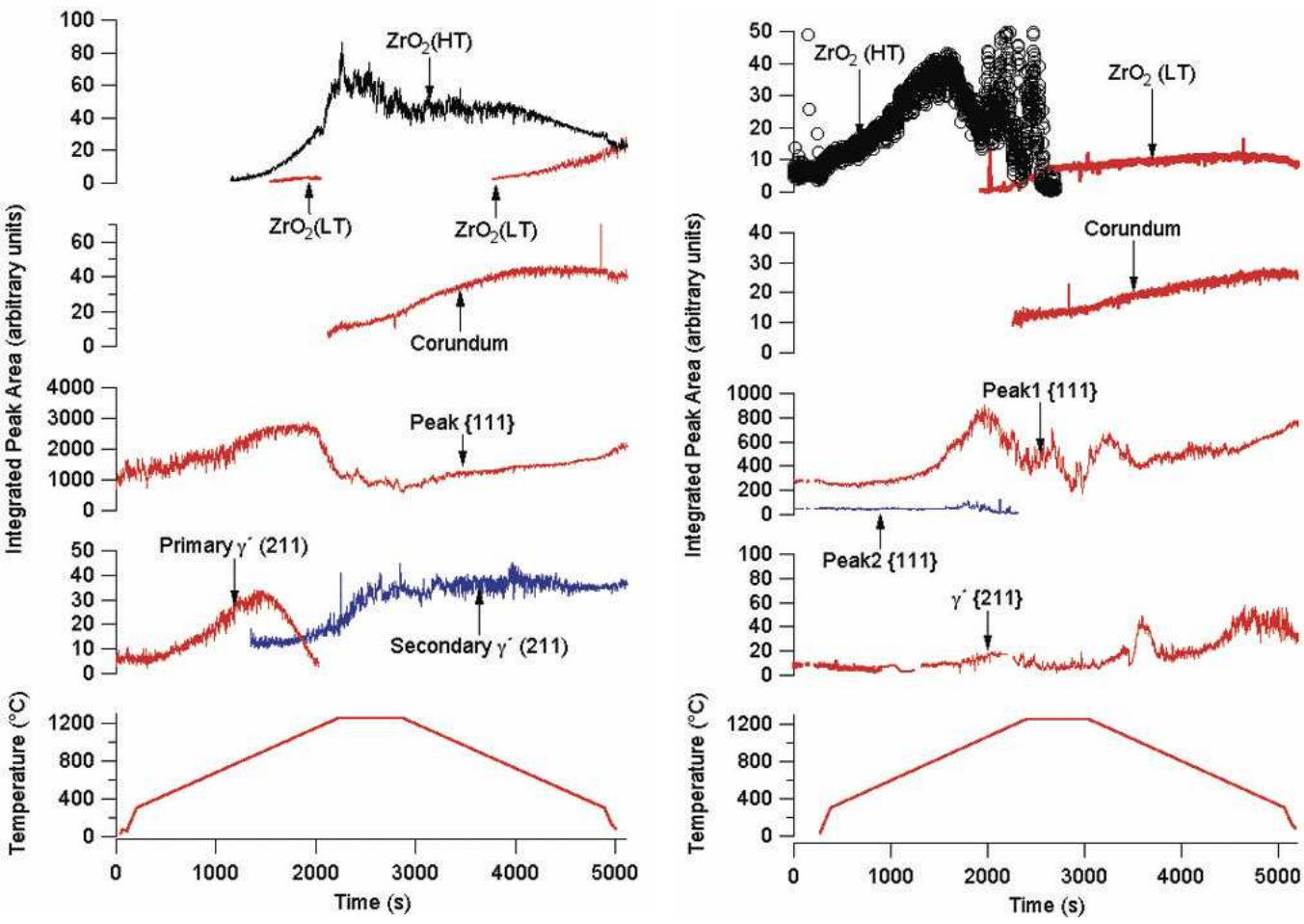

(*a*) (*b*)

Fig. 6—Summary of the analysis from TRXRD results: (*a*) and (*b*) the IC221M and Ni_3Al alloys, respectively, subjected to heating and cooling at a rate of 0.5 Ks^{-1}, and (*c*) and (*d*) the IC221M and Ni_3Al alloys, respectively, subjected to heating and cooling at a rate of 50 Ks^{-1}.

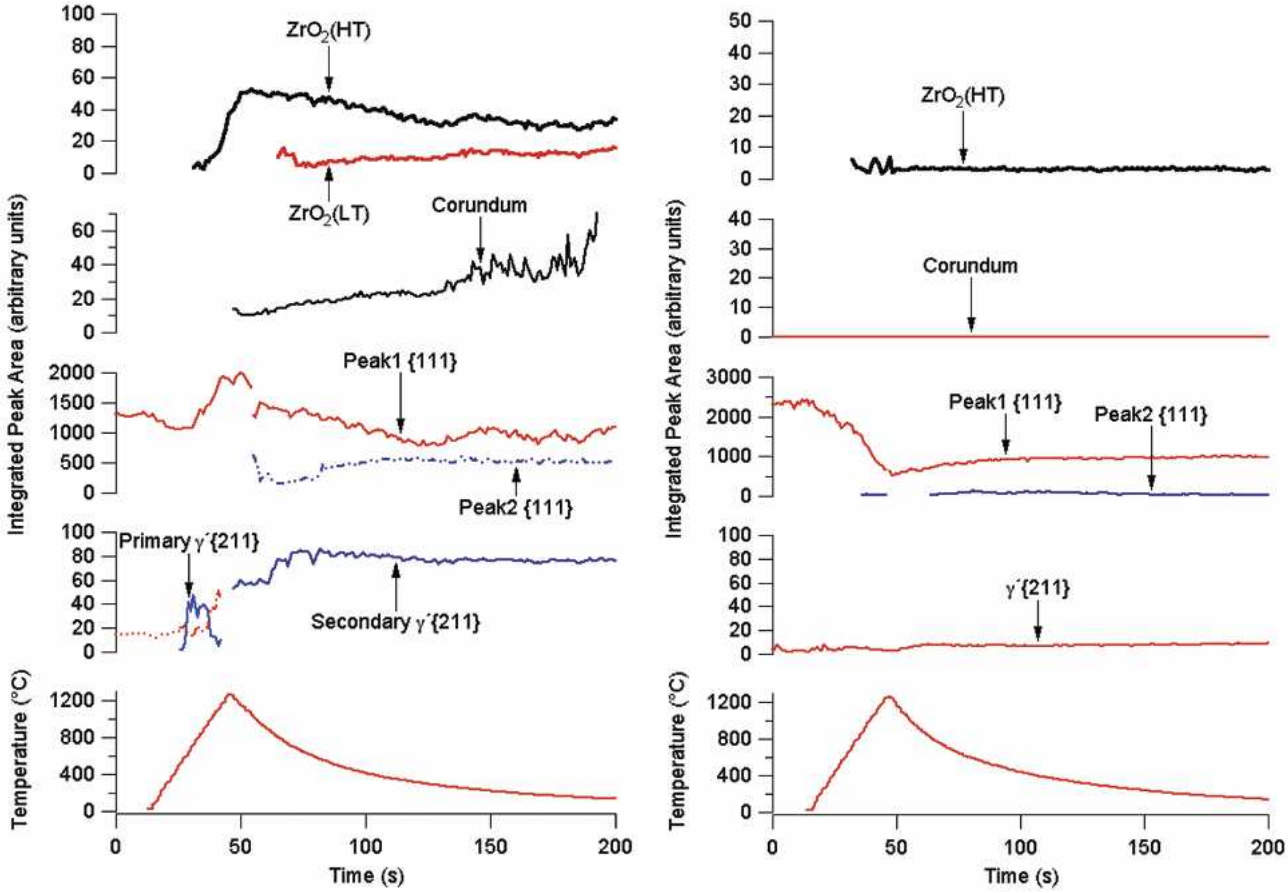

Fig. 6—(Continued). Summary of the analysis from TRXRD results: (*a*) and (*b*) the IC221M and Ni_3Al alloys, respectively, subjected to heating and cooling at a rate of 0.5 Ks^{-1}, and (*c*) and (*d*) the IC221M and Ni_3Al alloys, respectively, subjected to heating and cooling at a rate of 50 Ks^{-1}.

this again coincided with the rapid increase in the ZrO_2(HT) diffraction-peak area. The area under the (211) peak reached the maximum at 665 °C during cooling and then decreased only slightly below that temperature. The formation of Al_2O_3 was detected on reaching the peak temperature of 1250 °C. The peak area of Al_2O_3 continued to increase while holding at 1250 °C and also during cooling. The diffraction peak from ZrO_2(LT) appeared on cooling below 810 °C and continued to increase slightly. In this analysis, the splitting of the fcc (111) peak appeared in the cooling part of the cycle. As mentioned earlier, the interpretation of these peaks is difficult due to overlapping effects. In the next step, these oxidation characteristics are compared with those of the Ni_3Al alloys for a similar heat treatment.

In case of the R50 experiment on the Ni_3Al alloy (Figure 6(d)), the extent of oxidation was significantly reduced. Even though the faint presence of a ZrO_2(HT) diffraction peak was detected, the peak area did not change with this rapid heating and cooling experiment. The ZrO_2(LT) diffraction was not detected during the whole thermal cycle. The diffraction from Al_2O_3 phase was not detected. The change in the area of the (211) peak did not change. However, there was a decrease in the area under the (111) peak until the peak temperature was reached, which was closely related to the reduction in the width of the diffraction peak. However, on cooling, this change was less pronounced. The data also showed some tendency for the (111) peak splitting during heating and cooling. As mentioned earlier, this effect cannot be interpreted very easily. This is attributed to the recovery effect during the heating cycle. In the analysis of the data, the anomalous (211) diffraction peak (Figure 5(b)) was not considered.

It is interesting to note that in our analysis, diffraction information from the NiO or $NiO.Al_2O_3$ oxides was not detected. This is tentatively attributed to the low volume fraction of these oxides being below the sensitivity of the present technique. It is also possible that this is due to less time being spent in the temperature range of 600 °C to 800 °C, where the formation of NiO is favored,[8] in all our experimentation.

C. *Microstructure of Oxidized Samples*

The microstructures of the both IC221M and Ni_3Al alloys after the R0.5, R1, R10, and R50 experiments are compared in Figures 7(a) through (h). The results are presented in two groups, slow heating and cooling (R0.5 and R1) and rapid heating and cooling (R10 and R50).

The optical micrograph from the IC221M sample (Figure 7(a)) after the R0.5 experiment shows the presence of darkly etching oxides on the surface and in the interdendritic regions. The penetration depth of these oxides along

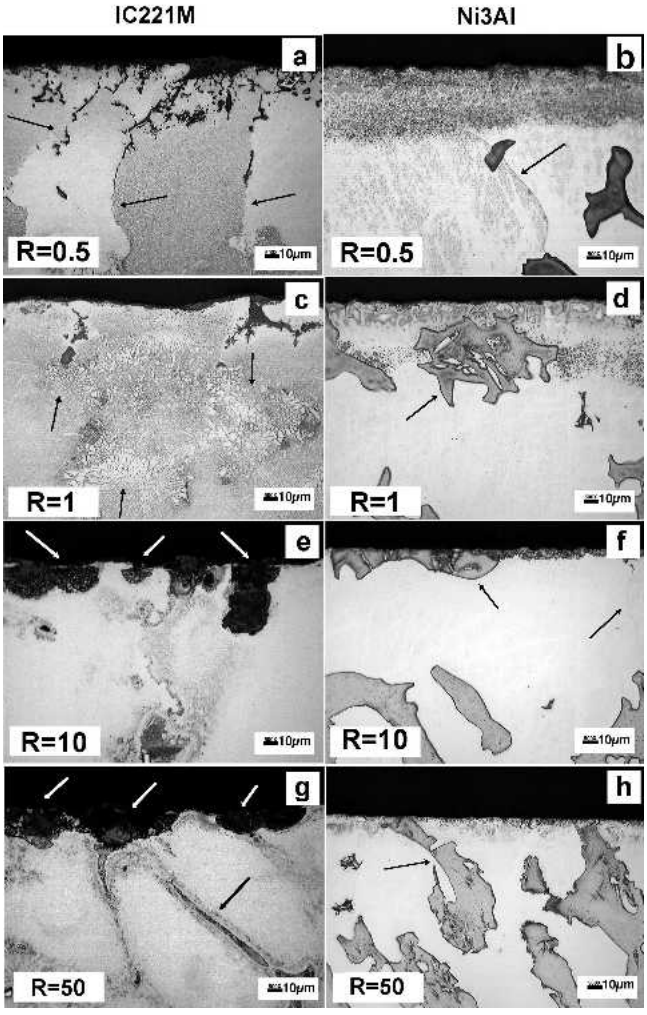

Fig. 7—Comparison of cross-sectional optical microstructures near the surface region of the sample close to the TRXRD investigation. The micrographs are identified by experimental condition: R0.5, R1, R10 and R50. The samples are in the etched condition and the etchant was aquaregia solution. The dendritic boundaries (black arrows) and liquation regions (white arrows) are marked.

the interdendritic boundaries is on the order of 50 to 60 μm. On comparing this microstructure with that of the as-cast microstructure (Figure 2(b)), a reduction of coarse γ' precipitates along the dendrite boundaries can be noticed. A similar oxide morphology was observed with an R1 experiment also (Figure 7(c)). The main difference between the IC221M samples, after the R1 and R0.5 experiments, was that the coarse γ' precipitates were persistent along the boundaries after the R1 experiment and were less persistent in the R0.5 experiment.

In case of the Ni_3Al sample subjected to the R0.5 experiment, a darkly etching fine distribution of oxides (Figure 7(b)) was observed near the surface. Moreover, there was a general tendency for the absence of darkly etching γ phase near the surface and within the sample. In the case of the Ni_3Al samples after the R1 experiment (Figure 7(d)), the extent of oxide formation appeared to be less, and the darkly etching γ phase was present near the surface.

The microstructures from the R10 and R50 experiments on the IC221M alloy showed large differences compared to the results from the R0.5 and R1 experiments. The most obvious result was that the extent and apparent penetration of oxides appeared to be larger than in the slow-heating experiments. In addition, both the microstructures suggest the tendency for liquidation along the dendrite grain boundaries. In this regard, it is noteworthy that during the R10 and R50 experiments on the IC221M alloys, small whiskers were observed on the surface of the samples. These whiskers are attributed to the gradual squeezing of the liquid from interdendritic boundaries and solidification of the same. These whiskers present a large surface per unit volume that leads to rapid oxidation. The rapid oxidation in the IC221M alloy during the R50 experiment is consistent with the TRXRD results presented in Figures 4 and 6. The microstructures from the Ni_3Al alloys, after the R10 and R50 experiments, showed very little difference. The extents of oxidation and depth of oxide penetration were very little. The presence of darkly etching γ phase was present even in the surface. The microstructure from the R50 experiment on the NI_3Al alloy is consistent with the lack of extensive oxide peaks in the TRXRD results.

It is important to stress that the microstructural analysis presented here is preliminary, and further detailed characterizations using analytical electron microscopy are underway to understand the oxides that form in the surface and also in the subsurface regions.

IV. DISCUSSION

An overview of the previously presented results indicated the following crucial phenomena. (1) In both the Ni_3Al and IC221M alloys under slow heating and cooling, the ZrO_2 formation occurs before the Al_2O_3 formation is detected. (2) With rapid heating and cooling, as expected, the Ni_3Al alloy did not show extensive oxidation and, in contrast, the IC221M alloy showed rapid oxidation. (3) In the IC221M alloy, an abrupt change in the lattice parameter of γ' was observed, in conjunction with the initiation of ZrO_2 formation. (4) In the Ni_3Al alloy, a metastable γ' formation was detected at high temperatures. In this section, the phenomena are rationalized based on the solidification microstructure and thermodynamic calculations.

A. *As-Cast Microstructure*

To understand the oxidation of these cast alloys, we need to understand the development of the as-cast microstructure in both alloys. The XRD and optical microscopy confirmed that the initial microstructures of the IC221M and Ni_3Al alloys are different. The IC221M alloy solidifies as a γ (fcc) phase, while the Ni_3Al alloy solidifies as a γ' ($L1_2$ ordered) phase. Thermodynamic calculations were performed to rationalize this microstructure evolution and to evaluate the effects of elemental segregation during casting.

The weight fractions of various phases for the IC221M alloy as a function of temperature were calculated (Figure 8(a)) using Thermo-Calc[17] software with the ThermoTech Ni-V6 database.[18] These equilibrium predictions indicate that in the chemically homogeneous alloy, the γ/γ' ratio varies considerably with temperature. Above about 1100 °C, γ phase is the predominant phase, while at lower temperatures,

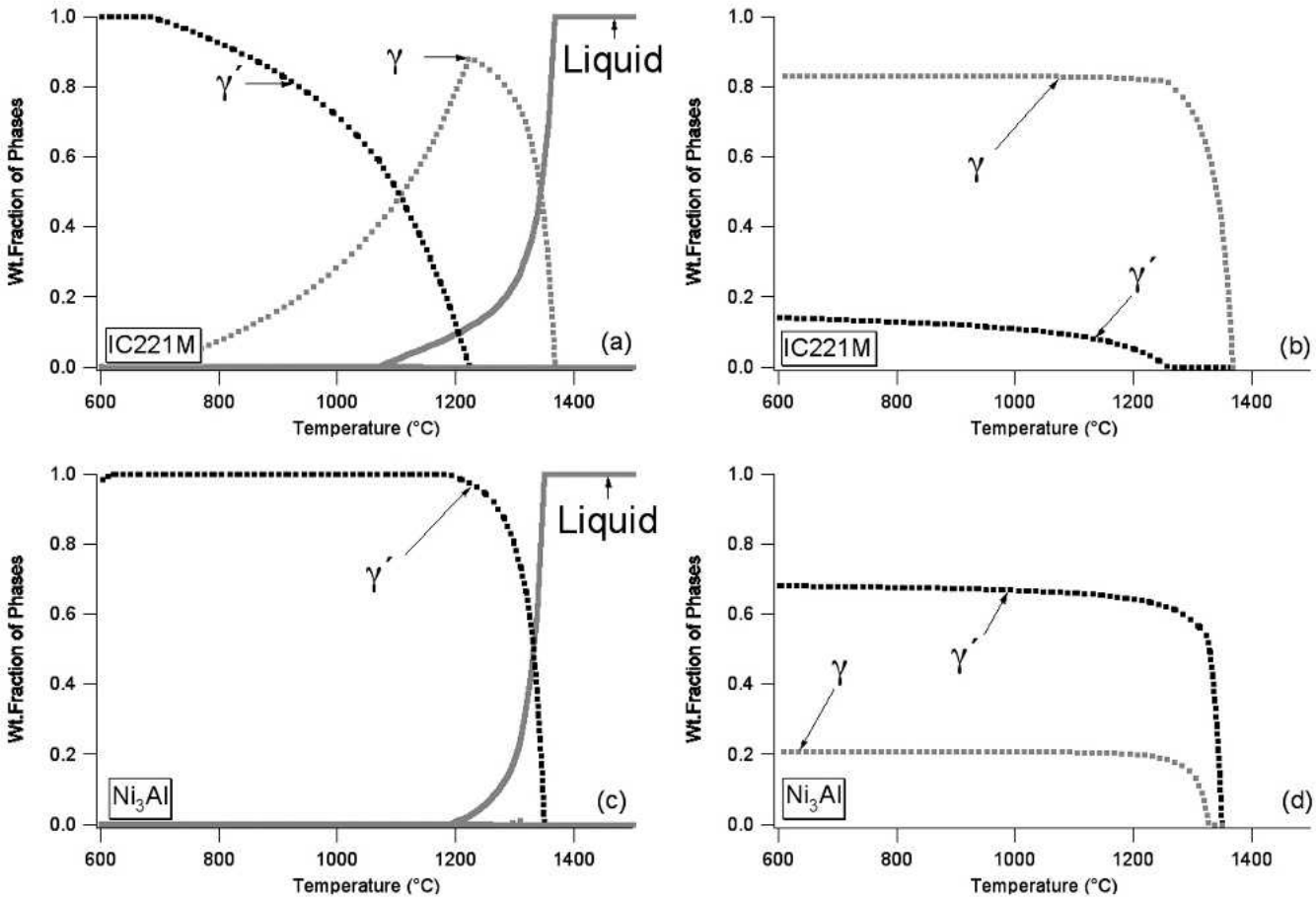

Fig. 8—Summary of equilibrium thermodynamic and solidification calculations from the IC221M and Ni_3Al alloys. (*a*) Predicted weight fraction of various phases in IC221M as a function of temperature. (*b*) Predicted weight fraction of various phases in IC221M during solidification as a function of temperature. (*c*) Predicted weight fraction of various phases in Ni_3Al as a function of temperature. (*d*) Predicted weight fraction of various phases in Ni_3Al during solidification as a function of temperature.

γ' phase predominates. The nonequilibrium microstructure produced by solidification of the cast alloy was assessed using a Scheil simulation.[17] Scheil simulations consider alloy solidification under conditions of no diffusion in solid and complete diffusion in liquid. The simulation predicts the microstructure at the temperature where solidification ends and a limiting case of elemental portioning between solid and liquid phases. For the IC221M alloy, the Scheil simulation results of Figure 8(b) confirm that γ is the first solid phase to form when solidification starts. At the end of solidification, the simulation predicts a microstructure of about 80 pct γ and 15 pct γ'. The remaining material will be Zr-enriched liquid that should solidify near 1170 °C to a eutectic constituent containing Ni_5Zr. As the γ phase cools after solidification, it will further transform to a mixture of $\gamma + \gamma'$, depending on its local composition.

In contrast, for the Ni_3Al alloys, the equilibrium calculation indicates that γ' is the most stable phase for the whole temperature range (Figure 8(c)). However, the Scheil simulation (Figure 8(d)), suggests that during solidification, about 20 pct of γ phase forms in the interdendritic regions. This is in agreement with the observed microstructure (Figure 2).

It is important to note these Scheil calculations indicated the preferential partitioning of Zr to the liquid due to limited solubility in the γ and γ' phases in both alloys. Based on these calculations, it is estimated that the last solidifying liquid may be enriched to a zirconium concentration greater than 30 wt pct. However, it is well known that a nickel-rich liquid containing a zirconium concentration of 8.8 wt pct may decompose at ~1175 °C into a Ni-Ni_5Zr eutectic mixture.[19] Lee *et al.*[7] has shown the proof for the presence of Ni_5Zr in the as-cast microstructure. Due to the limitations of thermodynamic data, the formation of this eutectic microstructure is not predicted in the calculations. Nevertheless, one can evaluate the extent of zirconium enrichment in the liquid as a function of solid weight fraction (Figure 9). The results show that the zirconium enrichment in the IC221M alloy is more extensive than that of the Ni_3Al alloys. Based on these calculations, approximately 18 wt pct of eutectic fraction can form in the IC221M alloys and, similarly, 8 wt pct of eutectic fraction can form in the Ni_3Al alloys. The eutectic microstructure was clearly evident in the IC221M alloys and is in agreement with the previous results. Although a fine microstructure was observed in the Ni_3Al alloys within the darkly etching γ regions in the as-cast state, further work is necessary to identify whether these morphologies correspond to a eutectic reaction. The previous calculations essentially indicate that the interdendritic regions of the IC221M alloys will be enriched in zirconium to a greater extent.

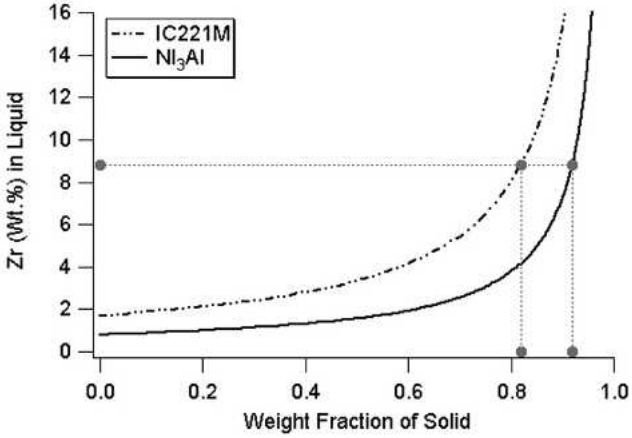

Fig. 9—Predicted concentration of liquid as a function of solid fraction solidified in (*a*) the IC221M alloy and (*b*) the Ni_3Al alloy. The calculations show higher enrichment of liquid with Zr for similar levels of solid fraction.

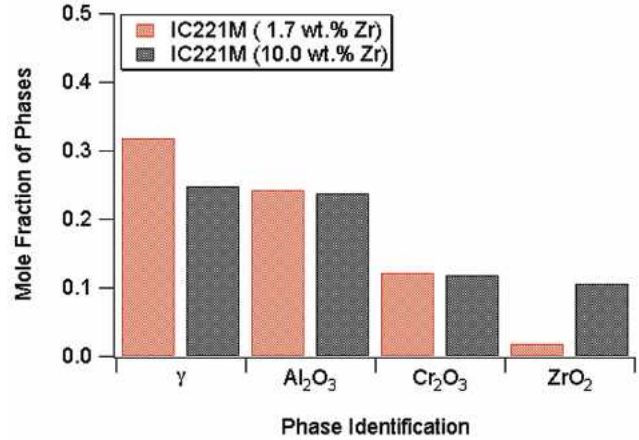

Fig. 10—Predicted mole fraction of different phases at 500 °C for two different concentrations of Zr for a given IC221M alloy.

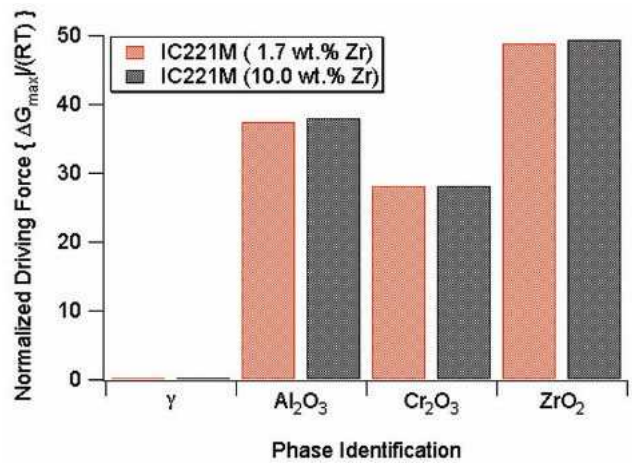

Fig. 11—Predicted variation of normalized driving force for different phase evolutions from a supersaturated γ phase for the same conditions as that used for Figure 10.

B. *Thermodynamic Calculation of Oxidation*

It is hypothesized that the zirconium enrichment in the interdendritic regions may allow for preferential formation of ZrO_2 compared to that of Al_2O_3. This hypothesis was tested by observing the thermodynamic stability of oxides in a Ni-Al-B-Cr-Mo-Zr-O-N system at 723 K. The activity of oxygen and nitrogen corresponding to dry air was calculated.* These activities of oxygen and nitrogen were set, and the stability of different oxides was calculated for the IC221 composition with two different zirconium concentrations (Figure 10). It is important to note that current thermodynamic data do not allow for the oxygen solution in the γ' phase. Therefore, we have assumed that the stability of the γ and γ' phases of similar composition will be the same with respect to the oxidation characteristics. A similar assumption was made for different allotropic forms of Al_2O_3 and ZrO_2. The calculations showed that for these conditions, Al_2O_3, Cr_3O_3, γ, and ZrO_2, are the most stable phases. In addition, the calculations also showed that the volume fraction of ZrO_2 was lower than that of other oxides (Figure 10) for the IC221 composition. To evaluate the effect of enhanced Zr segregation, the IC221M alloy with an increased to zirconium concentration (10 wt pct) was considered in the next step of the calculations. However, the calculations still predicted that the ZrO_2 oxide was present in the least amount. These calculations do not agree with the preferential formation of ZrO_2 oxide seen in the present experiments. This discrepancy can be rationalized based on kinetic constrictions.

*Only O_2 and N_2 were considered, and the presence of other species such as hydrogen is ignored.

Thermodynamic calculations do not consider the effect of kinetics and strictly predict the most stable oxide on reaching complete equilibrium. The kinetic constraints will be driven by the nucleation and growth of oxides on the surface. Since the nucleation rate is governed by the driving force for oxide formation, the next set of calculations considered the driving force for oxide formation with nominal and enriched zirconium concentrations. This is done by assuming that all oxides are in the dormant stage and calculating the maximum driving force for the formation of these oxides from a supersaturated solid solution. The results are shown in Figure 11. Interestingly, for both conditions, the driving force for the formation of ZrO_2 was found to be the maximum. It is well known that with the increase in driving force, the nucleation rate will be increased. These simple calculations illustrated that, under transient conditions, the early stages of oxidation will be determined by the nucleation rate of different oxides. This is also in agreement with the hypothesis presented by Lee *et al.*[7]

C. *Oxidation Characteristics of As-Cast Structure*

The previous calculations suggest that nucleation and growth characteristics must be important and, therefore, the oxidation characteristics under the slow (R0.5) and the fast (R50) conditions must be different.

The TRXRD showed slight differences in the rate of oxide formation in both the IC221M and Ni_3Al alloys, and microstructural observation showed some change in oxide morphology. In the IC221M samples, the oxidation in the interdendritic regions was observed. In contrast, in the Ni_3Al alloys, there is no such preferential oxidation in microstructures. The penetration of oxides from the surface was found to be higher in

the IC221M alloys compared to that of Ni_3Al alloys. Both these extents and the morphologies are attributed to the increased tendency for zirconium segregation in the IC221M alloy. The TRXRD data also showed the formation of secondary γ' phase during slow heating and cooling. Since this secondary γ' phase has a larger lattice parameter, it is speculated that this change is attributed to a large difference in the composition of γ' phase. This indicates that there are two competing reactions in the IC221M alloys. First, due to the increase in diffusivity with temperature, there will be a tendency to homogenize. The tendency for homogenization also can be inferred from the reduction of coarse γ' in the interdendritic region. Second, the zirconium segregation pattern that developed during solidification leads to preferential formation of ZrO_2(HT) first.

The current TRXRD results showed alumina formation in both the alloys at slow heating and cooling rates. In both the alloys, the alumina formation was enhanced above 1150 °C. However, at rapid heating rates, the alumina formation in Ni_3Al alloys was not detected.

Rapid heating and cooling rates showed that the oxidation characteristics are accelerated in the IC221M alloy compared to sluggish oxidation of the Ni_3Al alloy. Since the time spent at high temperature for both alloys was small, the extent of oxidation and diffusional homogenization should be less in both the alloys. The accelerated oxidation in the IC221M alloys is, indeed, a contradicting result. If the early stages of oxidation are driven by the nucleation and growth, the rate of oxidation should be sluggish in the IC221M alloy. Adding to the complexity, in the IC221M alloy, the peak area under the diffraction peaks of ZrO_2(HT), ZrO_2(LT), and Al_2O_3 are more or less similar to those measured at either slow or rapid heating and cooling rates. In contrast, no appreciable diffraction peak from Al_2O_3 was observed, and there was no change in the peak area of ZrO_2(HT) in the Ni_3Al alloys under rapid heating and cooling rates. This apparent anomaly was rationalized through the closer examination of the microstructure. The microstructures showed that there was evidence for incipient melting in the IC221M alloys, but not in the Ni_3Al alloys. This incipient melting is only possible in high heating rates, which allow for less time for the completion of solid-state decomposition of the Zr-enriched eutectic regions. The presence of zirconium-rich liquid will initiate a rapid oxide reaction from the liquid. This hypothesis, based on zirconium-rich liquid, is consistent with the observation that the TRXRD measured the ZrO_2 formation at 1100 °C only under rapid heating, while the Al_2O_3 reaction was measured only at 1250 °C.

The aforementioned results clearly show that the microstructural gradient with associated chemical heterogeneity would influence the early stages of oxidation to a greater extent, even under slow and rapid heating and cooling rates. In addition, the results suggest that Ni_3Al-based alloys are the most suitable for rapid thermal cycling conditions, due to a decreased tendency for preferential oxidation and incipient melting. In the case of the IC221M alloy, the results suggest that increased homogenization may be necessary to achieve uniform oxidation characteristics.

V. CONCLUSIONS

The primary solidification of a Ni-Al-Cr alloy (Ni_3Al alloy) with 12 wt pct Al occurred through the formation of γ' phase, and this mode of solidification leads to the presence of interdendritic γ phases. In contrast, the Ni-Al-Cr alloy with low aluminum (the IC221M alloy) solidified as primary γ phase, and the interdendritic regions were decorated with coarse γ' phase.

In-situ TRXRD during heating and cooling of these alloys in air identified the oxidation and change in phase stability as a function of temperature and time. During slow heating of the IC221M alloy in air at 0.5 Ks^{-1}, the area fraction of primary γ' phase increased at low temperatures. On continued heating, the formation of monoclinic ZrO_2 and tetragonal ZrO_2 was observed in conjunction with the formation of secondary γ' phase with a different lattice parameter. At the later stages of heating, with the formation of corundum and the continued formation of ZrO_2 and secondary γ' phase, the primary γ' phase disappeared. During cooling, the metastable tetragonal ZrO_2 decreased with the formation of monoclinic ZrO_2. The formation of primary and secondary γ' phase was observed in all heating and cooling conditions. The increased rate of oxidation even with a rapid heating rate is attributed to incipient melting of interdendritic Zr-enriched regions due to the lack of time for solid-state decomposition in these regions.

In Ni_3Al alloys, under slow heating and cooling conditions, the formation of both types of ZrO_2 as well as corundum was observed. However, under rapid heating and cooling conditions, the formation of monoclinic ZrO_2 and corundum was not observed. The results suggest that the Ni_3Al alloys may be more resistant to early stages of oxidation during rapid heating and cooling thermal cycles.

The aforementioned interactions between phase stability and oxidation characteristics are rationalized with computational thermodynamic calculations of microstructure evolution during solidification and stability of various phases in air.

ACKNOWLEDGMENTS

This research was sponsored by the Division of Materials Sciences and Engineering, United States Department of Energy, under Contract No. DE-AC05-00OR22725 with UT–Battelle, LLC. The UNICAT facility at the Advanced Photon Source (APS) is supported by the University of Illinois at Urbana–Champaign, Materials Research Laboratory (United States Department of Energy, the State of Illinois-IBHE-HECA, and the National Science Foundation), the Oak Ridge National Laboratory (United States Department of Energy under contract with UT-Battelle LLC), the National Institute of Standards and Technology (United States Department of Commerce), and UOP LLC. The APS is supported by the United States Department of Energy, Basic Energy Sciences, Office of Science under Contract No. W-31-109-ENG-38. The authors thank B.A. Pint, T.R. Watkins, and G. Muralidharan, Oak Ridge National Laboratory, for helpful comments on the manuscript.

REFERENCES

1. S.C. Deevi and V.K. Sikka: *Intermetallics*, 1996, vol. 4, pp. 357-75.
2. J.L. Smialek: *Surface and Interface Analysis*, 2001, vol. 31, pp. 581-92.
3. J.L. Smialek and R. Gibala: *Metall. Trans. A*, 1983, vol. 14, pp. 2143-61.
4. J.L. Smialek: *Metall. Trans. A*, 1987, vol. 18, pp. 164-67.

5. D. Lee, M.L. Santella, I.M. Anderson, and G.M. Pharr: unpublished research, 2004.
6. J. Klöwer, U. Brill, and U. Heubner: *Intermetallics*, 1999, vol. 7, pp. 1183-94.
7. D.B. Lee and M.L. Santella: *Mater. Sci. Eng.*, 2004, vol. A374, pp. 217-23.
8. J. Doychak: in *Intermetallic Compounds: Vol. 1. Principles*, J.H. Westbrrok and R.L. Fleishcer, eds., John Wiley and Sons Limited, 1994.
9. M.P. Brady *et al.*: *Materials Science and Technology, A Comprehensive Treatment, Volume II, Corrosion and Environmental Degradation*, M. Schütze, ed., Wiley-VCH Verlag GmbH, Federal Republic of Germany, 2000.
10. B.A. Pint: *Surface Coating Technol.*, 2004, vol. 188–89, pp. 71-78.
11. V. Kolarik, H. Fietzak, W. Engel, B. Eltester, and H.J. Grabke: *Mater. Sci. Forum*, 1997, vol. 252–54, pp. 251-58.
12. P.F. Tortorelli, K.L. More, E.D. Specht, B.A. Pint, and P. Zschack: *Materials at High Temperatures*, 2003, vol. 20, pp. 303-09.
13. E.D. Specht, P.F. Tortorelli, and P. Zschak: *Powder Diffraction*, 2004, vol. 19, pp. 69-73.
14. J.W. Elmer, T.A. Palmer, S.S. Babu, and E.D. Specht: *Mater. Sci. Eng. A*, 2005, vol. 391/1–2, pp. 104-13.
15. D.K. Smith and H.W. Newkirk: *Acta Crystallographica*, 1965, vol. 18, pp. 983-91.
16. B.C. Weber: *Acta Crystallographica*, 1962, vol. 15, p. 1187.
17. J.O. Andersson, T. Helander, L. Höglund, P.F. Shi, and B. Sundman: *Calphad*, 2002, vol. 26, pp. 273-312.
18. Thermotech Ni-Data Version 6, Thermotech Ltd./Sente Software Ltd., Surrey Technology Centre, 40 Occam Road, GU2 7YG, United Kingdom.
19. M.L. Santella: *Scripta Metall. Mater.,* 1993, vol. 28, pp. 1305-10.